

Plasmon thermal conductivity of thin Au and Ag filmsDong-min Kim, Jeongmin Nam, and Bong Jae Lee ^{*}*Department of Mechanical Engineering, Korea Advanced Institute of Science and Technology, Daejeon 34141, South Korea and Center for Extreme Thermal Physics and Manufacturing, Korea Advanced Institute of Science and Technology, Daejeon 34141, South Korea* (Received 27 July 2023; revised 6 October 2023; accepted 1 November 2023; published 17 November 2023)

We investigated the in-plane thermal conductivity of surface plasmon polaritons (SPPs) propagating along thin Au and Ag films on a SiO₂ substrate with a Ti adhesive layer. To determine the propagation length and skin depth of SPPs along Au and Ag thin films, we numerically solved the dispersion relation while considering the size effect of the permittivity of metal. Additionally, we derived the spatial distribution of SPPs along the film thickness to analyze the effect of the Ti adhesive layer on the plasmon thermal conductivity of Au and Ag thin films. Our theoretical predictions revealed a decrease of approximately 30% in plasmon thermal conductivity when considering the size effect of the permittivity of thin metal films. Furthermore, this causes the film thickness at which maximum thermal conductivity occurs to increase by about 30%. Taking these factors into account, we calculated the optimal thickness of Au and Ag films, along with Ti adhesive layers, on SiO₂ substrates to be approximately 20 nm. By fabricating a sample with the optimal thickness of Au and Ag films, we experimentally demonstrated that the plasmon thermal conductivity of Au and Ag films can be as high as about 20% of their electron contribution. This research will broaden the thermal design applications of ballistic thermal transport by SPPs propagating along thin metal coatings in microelectronics.

DOI: [10.1103/PhysRevB.108.205418](https://doi.org/10.1103/PhysRevB.108.205418)**I. INTRODUCTION**

For nanoscale thin films, the thermal conductivity of primary heat carriers such as phonons and electrons decreases as film thickness decreases due to their boundary scattering, which causes critical thermal issues for the performance of modern electronic devices [1]. In response to this issue of the classical size effect, recent research efforts have shifted their focus towards exploiting ballistic thermal transport facilitated by surface electromagnetic waves (SEWs), which emerge from the coupling of photons with either optical phonons (in polar dielectrics) or free electrons (in conductors), commonly referred to as polaritons, at the interface between differing media [2–6].

Initially, a substantial body of research has been dedicated to the exploration of radiative heat transfer mediated by SEWs, which has been the subject of extensive investigation in both far-field and near-field regimes [3,7–18]. Far-field thermal emission, which occurs for objects above absolute zero temperature, has been engineered through the utilization of controlled optical properties of nanostructures. The polar nanostructures that support SEWs have been effectively employed to manipulate thermal emissions [8,14,16,18]. However, it is imperative to acknowledge that far-field thermal emission remains constrained by the upper limit dictated by Planck's law. Conversely, when the separation distance between two objects becomes smaller than the thermal wavelength, radiative heat transfer between these objects can surpass this limit, a phenomenon commonly referred

to as the near-field thermal radiation [7]. Within phonon-polaritonic media, the evanescent component of SEWs, such as surface phonon polaritons (SPhPs), dominates near-field radiative heat transfer (NFRHT) along the cross-plane direction. Experimental validation of NFRHT enhancement through the utilization of planar polaritonic media has been established for nanoscale gaps [3,9–13,15,17].

Beyond the extensive investigations into radiative heat transfer facilitated by SEWs, recent attention has been directed towards conductive heat transfer mediated by SEWs and polaritons along films and interfaces [19,20]. By harnessing SEWs as additional heat carriers, it becomes possible to compensate for the classical size effect observed in the thermal conductivity of thin films, primarily attributed to their considerable propagation lengths that surpass those of the primary heat carriers in thin films by several orders of magnitude [21,22]. SPhPs, a specific class of SEWs generated through the coupling of photons with the optical phonons in polar materials, have been theoretically proposed to enhance the thermal conductivity of a 40-nm-thick SiO₂ membrane by over 100% compared to its bulk value [2].

Previous investigations have extensively explored the phenomenon of conductive thermal transport facilitated by SPhPs. Through analytical methods, Ordonez-Miranda *et al.* [4] demonstrated that the thermal conductivity of suspended polar membranes can be significantly enhanced, reaching up to 1.8 times its bulk counterpart, by carefully selecting substrate permittivity, film thickness, and temperature. Subsequent experimental studies corroborated the thermal conductivity of suspended membranes in relation to varying film thickness [23], temperature [24], and film width [25]. Practical implementation of SEWs in the thermal design of

^{*}bongjae.lee@kaist.ac.kr

electrical devices encounters great challenges when it comes to achieving the full potential of SPhPs because fabricating nanoscale-thick membranes larger than the propagation length of SPhPs is nearly impossible. Additionally, although SPhPs can propagate in supported multilayer polar films (i.e., an asymmetric medium), they exhibit well-confined behavior only when the thin film exceeds a characteristic thickness determined by the substrate and superstrate permittivity [5,6,26]. With such a thick film, the heat flux carried by SPhPs becomes insignificant.

In contrast, surface plasmon polaritons (SPPs) represent an alternative form of SEWs and can also serve as heat carriers in conductive heat transfer. SPPs arise from the interaction of photons with free electrons in metals. Unlike polar dielectric films, long-range SPPs can propagate over centimeters on “supported” metallic nanofilms in the midinfrared regime [21,22]. Due to the high plasma frequency and large negative value of the real part of the metal permittivity, the frequency range of metal films that support SPPs (i.e., $\omega < \omega_p/\sqrt{2}$) is broader compared to that of polar dielectric films [27]. The inherent characteristics of long-range SPPs offer the potential for achieving complete propagation over a wide spectrum range, with the expectation of significantly augmenting thermal transport within thin metal films. Additionally, the investigation of SPP propagation along the interfaces between metallic film patterns and the surrounding dielectric media has been a subject of intensive scrutiny in prior research endeavors [28–33]. However, while the broad frequency range of SPPs holds potential for enhancing heat conduction in metal films, previous studies primarily focused on the propagation and thermal effects of SPPs at specific frequencies, overlooking the broader spectral characteristics. Recently, Kim *et al.* [34] demonstrated the enhanced in-plane thermal conductivity of a Ti film by exploiting the long-range SPPs. It was shown that the plasmon thermal conductivity of a 100-nm-thick Ti film can contribute to additional energy transport by 25% of its intrinsic thermal conduction by electrons and phonons. Despite the potential to achieve full propagation of SPPs on supported films, Ti films still face limitations in addressing thermal issues in microelectronics due to their low intrinsic thermal conductivity.

Alternatively, Ordonez-Miranda *et al.* [27] theoretically investigated the plasmon thermal conductivity of a gold nanofilm on a silicon substrate, considering the effects of film thickness and temperature. They revealed that the plasmon thermal conductivity reaches about 25% of its electron counterpart. However, experimental verification of the plasmon thermal conductivity in noble metal films, such as Au and Ag, necessitates additional considerations. First, the use of SiO₂ as a substrate is recommended to accurately measure the in-plane thermal conductivity of nanoscale metal films, as the low phonon thermal conductivity of SiO₂ enhances the measurement sensitivity [34]. Second, the influence of an additional adhesive layer (e.g., Ti) on the dispersion of SPPs should be taken into account, particularly because noble metals exhibit poor adhesion to a SiO₂ substrate. Lastly, it is crucial to analyze the size effect of permittivity and its impact on the plasmon thermal conductivity, given that the film thickness at the maximum plasmon thermal conductivity

for Au (≈ 10 nm [27]) is certainly shorter than the mean free path of electrons (≈ 50 nm).

In this paper, we measure the plasmon thermal conductivity of nanoscale Au and Ag films deposited on a SiO₂ substrate with a Ti adhesive layer. The dispersion relation of SPPs propagating along the Au and Ag thin films is determined through numerical analysis, taking into account the thickness-dependent behavior of metal permittivity. Additionally, we examine the influence of the Ti adhesive layer on the SPP thermal conductivity as well as the thickness of Au and Ag films that lead to the maximum plasmon thermal conductivity. We achieve this by deriving the spatial distribution of SPPs along the films that incorporate the Ti adhesive layer. Through the fabrication of a sample with optimized Au and Ag film thicknesses, we conduct experimental investigations to explore the dependence of plasmon thermal conductivity on film thickness and radius.

II. THEORETICAL MODEL

The calculation of plasmon thermal conductivity as a function of film thickness involved numerically solving the dispersion relation of SPPs propagating along the films. The dispersion relation for SPPs supported by a single metal film on a SiO₂ substrate (i.e., no Ti adhesive layer) can be expressed [5]:

$$\tanh(p_m d) = -\frac{p_m \varepsilon_m (p_a \varepsilon_s + p_s \varepsilon_a)}{p_m^2 \varepsilon_a \varepsilon_s + p_a p_s \varepsilon_m^2}, \quad (1)$$

where d is the thickness of the metal film. The subscripts m , a , and s represent the metal, air, and substrate, respectively, while p_i denotes the cross-plane wave vector of the respective medium. The dispersion relation is valid regardless of film width because it was derived from tangential components of electric and magnetic fields at the film interfaces [27,35]. The permittivity of each medium, denoted as ε_i , is used to numerically obtain the in-plane wave vector β that satisfies $p_i^2 = \beta^2 - \varepsilon_i k_0^2$ for each medium. We employed the renowned Powell method as part of the shooting methods for numerical computation, based on the GNU Scientific Library (GSL), which is a collection of numerical computing routines crafted in the C++ programming language. The GSL provides the multidimensional root-finding algorithm that solves the equation by minimizing the function using its derivative [36].

The permittivity of “bulk” Au and Ag over a range of frequencies was predicted theoretically using the Drude model, i.e.,

$$\varepsilon_{\text{bulk}} = 1 - \frac{\omega_p^2}{\omega^2 + i\omega\Gamma}. \quad (2)$$

Here, the Drude model parameters, namely, the damping coefficient Γ and plasma frequency ω_p , were fitted to the tabulated data [37–39] using the least-squares method. The data from Palik [39] cover a spectral range exceeding 190 Trad s⁻¹, so the Drude parameters were determined by fitting the data from Ordal *et al.* [37,38] below 190 Trad s⁻¹. As a result, the Drude parameters for Au were determined as $\Gamma = 252$ cm⁻¹ and $\omega_p = 64\,660$ cm⁻¹, while for Ag, they were $\Gamma = 145$ cm⁻¹ and $\omega_p = 72\,071$ cm⁻¹. Since the permittivity of both data

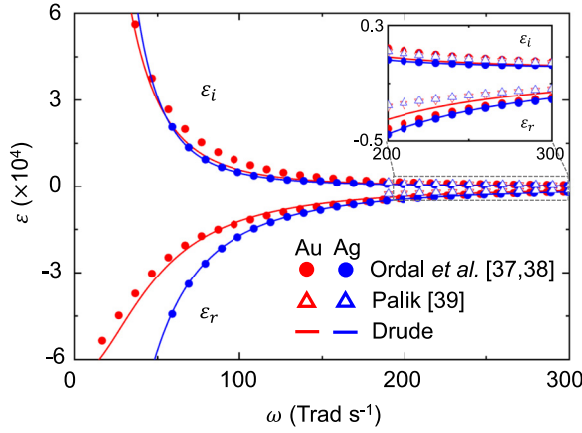


FIG. 1. Fitting of the Drude model to the existing experimental data of Au and Ag (bulk).

sets [37–39] matches better in the imaginary part than in the real part, the theoretical prediction of the real part of the permittivity based on the Drude model falls between the measurement data from Ordal *et al.* [37,38] and Palik [39], and the imaginary part of the permittivity agrees well with both data sets (refer to inset of Fig. 1). In addition, the permittivity of the SiO₂ substrate is determined using the tabulated data [39].

The plasmon thermal conductivity of a metal film on a silicon dioxide (SiO₂) substrate can be calculated using kinetic theory (KT) based on the Boltzmann transport equation (BTE) with diffusion approximation [2]:

$$k_{\parallel, \text{SPP}} = \frac{1}{4\pi d} \int_0^\infty k_\omega d\omega = \frac{1}{4\pi d} \int_0^\infty \hbar \omega \Lambda_{\text{eff}} \beta_R \frac{df_0}{dT} d\omega, \quad (3)$$

where \hbar is the Planck constant divided by 2π , ω is the angular frequency, and f_0 corresponds to the Bose-Einstein distribution function. Thermal transport via SPPs had also been demonstrated by using fluctuational electrodynamics (FE) in our previous work, which took into account the full-wave nature of SEWs [34]. Since the calculated propagation length of SPPs excellently agrees with both KT and FE, the diffusion approximation of the KT is believed to be valid in this paper. The real part of the in-plane wave vector is denoted as β_R , and the propagation length of SPPs is defined as $\Lambda = 1/(2\beta_I)$ with β_I being the imaginary part of the in-plane wave vector. The in-plane wave vector β can be obtained by solving Eq. (1). Finally, the effective propagation length (Λ_{eff}) for a metal film with a finite width L is predicted by the BTE [40]. The transmission t of SPPs can be defined by analytically solving the heat flux via SPPs along the film with the BTE. The effective propagation length Λ_{eff} of SPPs in the film with length L can be expressed with t as [40]

$$\Lambda_{\text{eff}} = t\Lambda = \left(1 - \frac{4\psi(0)}{\pi\mu}\right)\Lambda \quad (4)$$

where $\mu = L/\Lambda$, and $\psi(\xi) = E_5(\xi) - E_5(\mu - \xi)$ with $E_n(x) = \int_0^{\pi/2} \cos^{n-2}(\theta) e^{-x/\cos(\theta)} d\theta$ is a positive function with values between zero and unity, where θ is the angle between SPP propagation direction and $+z$ axis, and $\xi = z/\Lambda$. The Λ_{eff} obtained from the BTE considers the boundary scattering

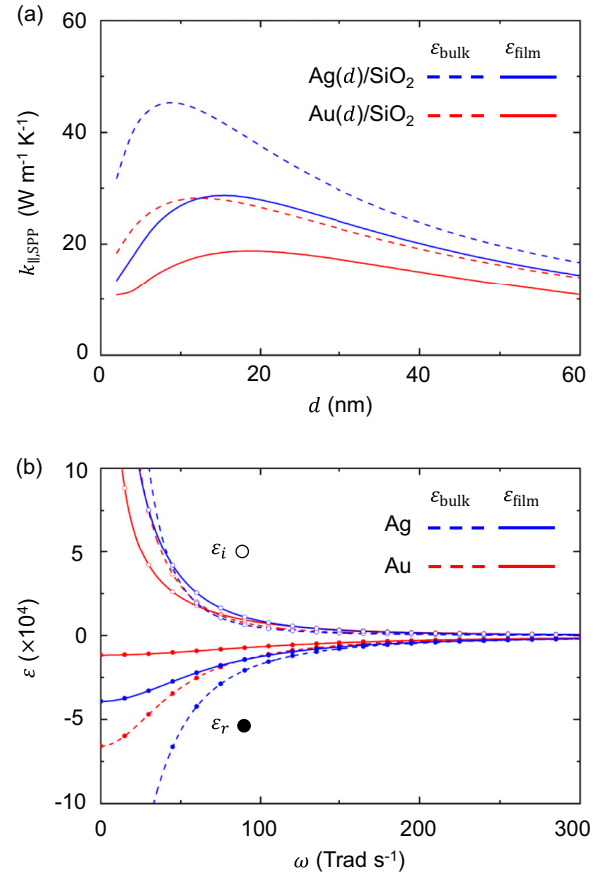


FIG. 2. (a) Calculated plasmon thermal conductivity of Au and Ag films directly deposited on a SiO₂ substrate with respect to film thickness when $L = 50$ nm. (b) Real (ϵ_r) and imaginary (ϵ_i) part of permittivity when $d = 16$ nm. Dashed lines are calculated based on the bulk permittivity of Au and Ag in Eq. (2), and solid lines are calculated based on the thin-film permittivity of Au and Ag with consideration of the size effect in Eq. (5).

more accurately than the semiempirical Matthiessen rule ($\Lambda_{\text{eff}}^{-1} = \Lambda^{-1} + L^{-1}$), thus expected to predict the $k_{\parallel, \text{SPP}}$ more precisely than the latter rule, as detailed in Guo *et al.* [40].

Using the bulk permittivity in Eq. (2), the dashed lines in Fig. 2(a) show how the plasmon thermal conductivity of Au and Ag films directly deposited on a SiO₂ substrate (no Ti adhesive layer) changes with their thickness when $L = 50$ nm. Here, the film width of 50 nm was deliberately selected to ascertain the upper limit of achievable plasmon thermal conductivity during the experimental validation process. Since the dispersion relation remains unaffected by variations in film width, the discussions presented in this paper remain applicable without regard to the specific film width. At first, a quick comparison with the plasmon thermal conductivity of a Ti film on a SiO₂ substrate [34] shows that the maximum plasmon thermal conductivity of Au and Ag films is more than ten times higher than that of the Ti film. Furthermore, the corresponding thickness of Au and Ag films is approximately seven times smaller than that of the Ti film. Remarkably, both Au and Ag films exhibit their maximum plasmon thermal conductivity at a thickness of approximately 10 nm. Considering that the plasmon thermal conductivity in thin metal

films increases as the SPPs at both interfaces of the metal film are decoupled [34], these findings suggest that SPPs are less confined in Au and Ag films compared to Ti films. This indicates a shorter penetration depth into the metal and a deeper propagation into lossless air for Au and Ag films, implying a longer propagation length for SPPs and thus a higher plasmon thermal conductivity compared to Ti film.

According to Gall [41], the mean free path of electrons in Au is approximately 37.7 nm, while in Ag, it is approximately 53.5 nm. This implies that the boundary scattering of electrons within Au and Ag films, which is thickness dependent, can result in variations in their permittivity. Thus, it becomes essential to account for this thickness-dependent permittivity when calculating the plasmon thermal conductivity. In the Drude model, the damping coefficient Γ is inversely proportional to the relaxation time τ , which represents the average time electrons travel between collisions [42]. Specifically, the electron mean free path (l) can be expressed as $l = v_F \tau$, where v_F denotes the Fermi velocity. In bulk metals, the electron mean free path is determined by the relaxation times associated with electron-electron, electron-phonon, and electron-defect scatterings. However, in noble metals like Au and Ag, electron-electron scattering plays a dominant role [43]. When considering thin films, electron-boundary scattering becomes significant, and the electron mean free path in a thin film (l_{film}) can be effectively described by [42]

$$\frac{l_{\text{film}}}{l_{\text{bulk}}} = \left(1 + \frac{\text{Kn}}{\ln(\text{Kn}) + 1}\right)^{-1}, \quad (5)$$

where l_{bulk} is the *bulk mean free path* of electrons and $\text{Kn} = l_{\text{bulk}}/d$ represents the Knudsen number with d being the film thickness. Using Eq. (5), we can obtain the modified damping coefficient of the Drude model for a thin metal film by $\Gamma_{\text{bulk}}/\Gamma_{\text{film}} = l_{\text{film}}/l_{\text{bulk}}$.

Solid lines in Fig. 2(b) show the predicted permittivity $\varepsilon_{\text{film}}$ of a 16-nm-thick Au and Ag film by considering the size effect based on Γ_{film} . The real part of the thin-film permittivity exhibits a significant reduction in the frequency range below 100 Trad s^{-1} . Due to the reduced permittivity of Au and Ag films, the maximum value of the plasmon thermal conductivity when using $\varepsilon_{\text{film}}$ is approximately 30% lower compared to that calculated with $\varepsilon_{\text{bulk}}$, as shown in Fig. 2(a). Additionally, the film thickness at which the maximum plasmon thermal conductivity occurs for Au and Ag films, based on $\varepsilon_{\text{film}}$, is approximately 30% larger than that based on $\varepsilon_{\text{bulk}}$. Figure 2 provides clear evidence that the effects of electron-boundary scattering must be considered when modeling the permittivity for the purpose of analyzing the plasmon thermal conductivity of a noble metal film. On the other hand, plasma frequency may have a nonlocal effect under film thickness below 10 nm due to the out-of-plane confinement of electrons [44–46]. The nonlocal effect of the plasma frequency was safely neglected for our experiments and analysis since the plasma frequency negligibly varies at a film thickness of 20 nm and shows a reduction under 10% of its value until its thickness is below about 3 nm for both Au and Ag (see Sec. 1 of the Supplemental Material [47]).

In order to examine the relationship between plasmon thermal conductivity and film thickness, which also affects the

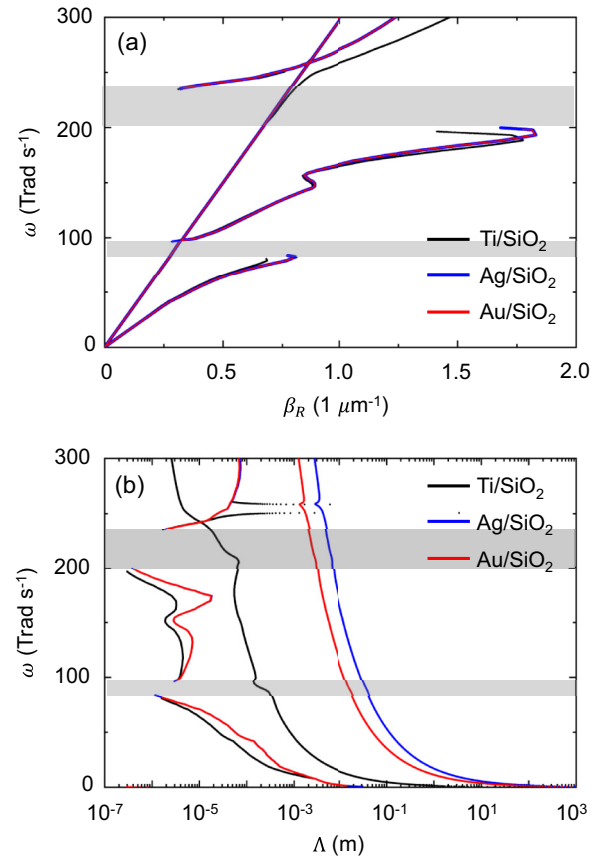


FIG. 3. (a) Real part of the in-plane wave vector of SPPs for 16-nm-thick Au, Ag, and Ti films directly deposited on a SiO_2 substrate. The shaded region indicates the frequency range where the real part of the dielectric function of the SiO_2 substrate becomes negative. (b) Propagation length of SPPs for 16-nm-thick Au, Ag, and Ti films directly deposited on a SiO_2 substrate.

permittivity, Fig. 3 illustrates the behavior of the real part of the in-plane wave vector β_R and the propagation length Λ_{eff} for Au, Ag, and Ti films directly deposited on a SiO_2 substrate (i.e., no adhesive layer) when $d = 16$ nm. The SPP dispersion curves are depicted within a frequency range from 0 to 300 Trad s^{-1} , as the spectral plasmon thermal conductivity of the metal films is primarily concentrated below 300 Trad s^{-1} [34]. These dispersion curves originate from the light line of the surrounding media, namely, $\omega/c = \varepsilon_{a,s} k_0^2$. That is, two modes of SPPs that originate from the interfaces between metal and surrounding dielectrics contribute to the plasmon thermal conductivity. Both modes are distinguished by symmetric and antisymmetric spatial distributions of the magnetic field [48]. The propagation length and penetration depth of both modes are strongly governed by the permittivity of the surrounding dielectrics. For a metal film with an asymmetric configuration (i.e., superstrate is not equal to substrate), the symmetric mode of SPPs that has a longer propagation length propagates along the interface between metal and dielectric with a lower refractive index [23]. Considering that thermal transport via SPPs in metal films is predominantly governed by the metal-air interface [34], the focus is primarily on the propagation of SPPs along the metal-air interface. Although

it is not noticeable from Fig. 3(a), β_R of Au and Ag films is closer to the light line of air than that of Ti film. Also, noble metals usually have low losses compared to refractory metals. Consequently, the propagation length of SPPs along the metal-air interface is approximately two orders of magnitude longer for Au and Ag films compared to Ti film, as depicted in Fig. 3(b).

Because β_R approaches the light line of air (i.e., $\beta_R \sim k_0$) for the SPPs propagating along the metal-air interface, the real part of the cross-plane wave vector can be approximated as $p_m \sim k_0\sqrt{1 - \varepsilon_{\text{film}}}$. Given that the permittivity of the metal is significantly larger than that of air (i.e., $\varepsilon_{\text{film}} \gg 1$), the penetration depth of SPPs into the metal is primarily determined by the real part of the metal permittivity, i.e., $\delta_m = 1/[2\text{Re}(p_m)] \approx 1/[2\text{Re}(k_0\sqrt{-\varepsilon_{\text{film}}})]$. Consequently, the penetration depth of SPPs into Ti film is longer compared to Au and Ag films, because the real part of the Ti permittivity is much smaller than the real part of the Au and Ag permittivity. Therefore, the film thickness at which the maximum plasmon thermal conductivity occurs is much smaller for Au and Ag films compared to Ti film, as the maximum occurs when SPPs at both interfaces are decoupled (i.e., $d \approx 2\delta_m$). Due to the above reasons, Au and Ag films directly deposited on a SiO₂ substrate achieve the maximum plasmon thermal conductivity with the smaller film thickness compared to Ti films, as depicted in Fig. 2(a).

The plasmon thermal conductivity of the Au and Ag films, as demonstrated in Fig. 2(b), exhibits a diminished peak value and an increased film thickness at the point of maximum conductivity when $\varepsilon_{\text{film}}$ is employed. The reduction in plasmon thermal conductivity can be explained quantitatively by examining the dispersion curves depicted in Fig. 3(a). These dispersion curves for β_R closely coincide with the analytical solutions representing the dispersions of SPPs at the single interface between a metal and its surrounding medium [34]. The expressions for these dispersions are simply given by

$$\beta_{a,s} = \varepsilon_{a,s}^{1/2} k_0 \left(\frac{\varepsilon_{\text{film}}}{\varepsilon_{\text{film}} + \varepsilon_{a,s}} \right)^{1/2}, \quad (6)$$

where β_a and β_s represent the in-plane wave vectors at the metal-air and metal-substrate interfaces, respectively. Assuming that β_R is significantly greater than β_I , the imaginary part of the in-plane wave vectors at each interface can be expressed by [21]

$$\beta_{a,st} = \frac{1}{2} \frac{\varepsilon_{a,s}^2 \text{Im}(\varepsilon_{\text{film}})}{\beta_{a,sR}} \frac{k_0^2}{|\varepsilon_{\text{film}} + \varepsilon_{a,s}|^2}, \quad (7)$$

where $\text{Im}()$ takes the imaginary part. Because the plasmon thermal conductivity is proportional to β_R/β_I , as indicated in Eq. (3), and remains within the same order of magnitude across film thicknesses ranging from 0 to 60 nm [see Fig. 2(a)], it is reasonable to perform a quantitative analysis of the plasmon thermal conductivity using Eq. (7). This analysis holds true regardless of whether the film falls under the category of thin or thick films, i.e., the coupled/decoupled regime.

As the film thickness decreases (resulting in an increase in Γ_{film}), the metal permittivity $\varepsilon_{\text{film}}$ decreases for both the real and imaginary parts. By assuming that ω_p is much greater than Γ_{film} and by analytically separating the real and

imaginary components of the Drude model from Eq. (2), it can be observed that the real part of $\varepsilon_{\text{film}}$ is inversely proportional to Γ_{film}^2 , while the imaginary part of $\varepsilon_{\text{film}}$ is inversely proportional to Γ_{film} . Hence, as the size effect leads to an increase in Γ_{film} , the propagation length of SPPs on the metal-air interface diminishes, thereby causing a decrease in the plasmon thermal conductivity. This reduction can be attributed to the amplified β_{aI} term [as shown in Eq. (7)], primarily driven by the dominant increase in $\varepsilon_{\text{film}}$. Furthermore, the increase in film thickness at the point of maximum plasmon thermal conductivity can also be elucidated by considering the skin depth of SPPs within the metal film. As mentioned previously, the skin depth in the metal film, denoted as δ_m , is inversely proportional to the real part of $\varepsilon_{\text{film}}$. Consequently, considering the size effect, which leads to a decrease in the absolute value of the real part of $\varepsilon_{\text{film}}$, results in a slight augmentation of δ_m . A larger δ_m signifies that a greater film thickness is necessary for the decoupling of SPPs at the interface. Therefore, when accounting for the size effect of the metal permittivity in thin films, the film thickness at the point of maximum plasmon thermal conductivity increases.

III. RESULTS AND DISCUSSION

The relatively low thermal conductivity of SiO₂ enhances the measurement sensitivity of in-plane thermal conductivities in Au and Ag films by concentrating the heat transfer pathway on the metal films. However, due to the weak adhesion between the Au and Ag films and the SiO₂ substrate, an additional Ti adhesive layer must be deposited between the metal films and the substrate. It is necessary for the Ti adhesive layer to have a minimum thickness of 10 nm to ensure sufficient adhesive force. By solving the dispersion relation of SPPs with the presence of the Ti adhesive layer, we determined the film thickness at which the maximum plasmon thermal conductivity occurs for the Au and Ag films. The dispersion relation of SPPs in a four-layer structure can be expressed as follows [5]:

$$\frac{\tanh(p_1 d_1) + \alpha_{01}}{1 + \alpha_{01} \tanh(p_1 d_1)} = -\alpha_{21} \frac{\tanh(p_2 d_2) + \alpha_{32}}{1 + \alpha_{32} \tanh(p_2 d_2)}, \quad (8)$$

where the subscript i denotes the i th medium (i.e., $i = 1, 2, 3, 4$), and $\alpha_{ij} = \varepsilon_i p_j / \varepsilon_j p_i$. By substituting the solved value of β from Eq. (8) into Eq. (3), the calculated plasmon thermal conductance $G = k_{\parallel, \text{SPP}} d$ of Au and Ag films with a Ti adhesive layer is plotted in Fig. 4(a). Since the Ti adhesive layer has a negligible effect on the dispersion of SPPs, the thermal conductance of SPPs is nearly the same regardless of whether the Ti adhesive layer exists. Also, the calculated plasmon thermal conductivity of Au and Ag films with a Ti adhesive layer is plotted in Fig. 4(b). Upon introducing a 10-nm-thick Ti adhesive layer between the Au and Ag films and the substrate, the plasmon thermal conductivity decreases by approximately 25%, and the film thickness at which the maximum plasmon conductivity occurs increases by around 30%.

The impact of the Ti adhesive layer on the plasmon thermal conductivity can be explained by considering the skin depth of SPPs within the metal (δ_m). Figure 4(c) illustrates the skin depth of SPPs in the 10-nm-thick Ti adhesive layer when the

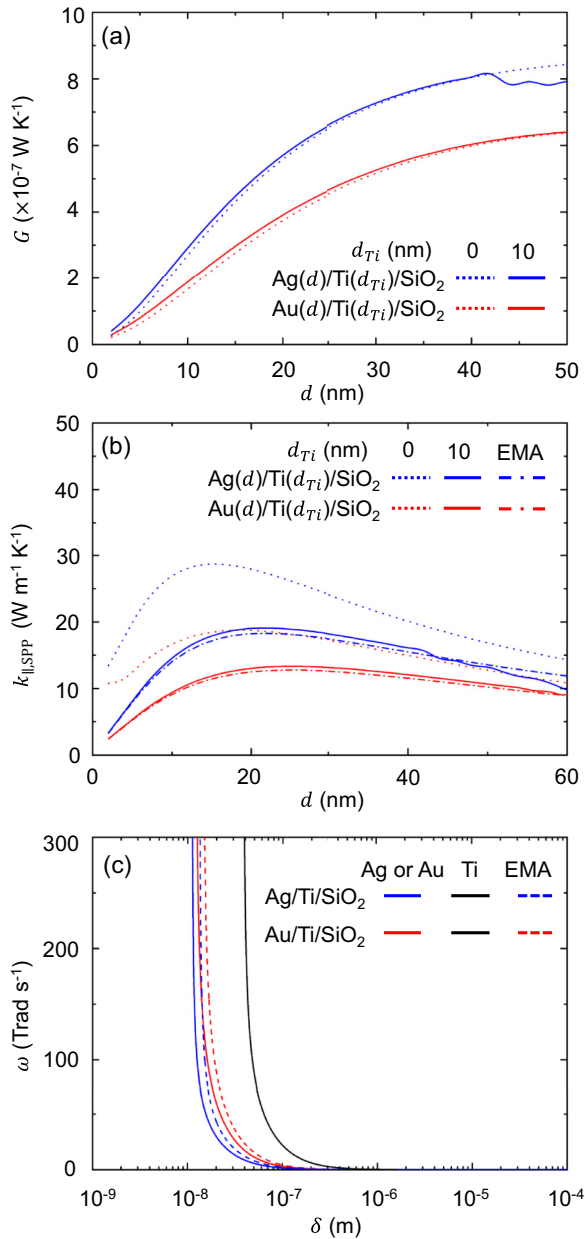


FIG. 4. (a) Plasmon thermal conductance of Au and Ag films on a SiO₂ substrate with respect to their thickness. (b) Plasmon thermal conductivity with respect to Au and Ag film thickness on a SiO₂ substrate with a 10-nm-thick Ti adhesive layer. “EMA” represents the calculated plasmon thermal conductivity of the effective medium consisting of Au or Ag film and a Ti adhesive layer by using the effective medium approximation. (c) Skin depth of SPPs along 20-nm-thick Au and Ag films, and a 10-nm-thick Ti adhesive layer.

film thickness of Au and Ag films is 20 nm. For frequencies above 200 Trad s⁻¹ (corresponding to the peak wavelength of the Planck distribution at 300 K), the skin depth of SPPs in the Ti adhesive layer exceeds 40 nm. Consequently, there is relatively little attenuation of SPPs within the Ti adhesive layer. In other words, the dispersion of SPPs along the metal films is expected to be negligibly affected by the Ti adhesive layer. Considering that the majority of thermal transport through SPPs occurs at the metal-air interface, the presence

of the Ti adhesive layer primarily influences the overall film thickness used in the calculation of plasmon thermal conductivity in Eq. (3). As a result, the plasmon thermal conductivity decreases since it is inversely proportional to the overall film thickness. Conversely, the film thickness at which the maximum plasmon thermal conductivity occurs increases with the Ti adhesive layer due to the augmented effective skin depth within the metal films. To estimate the effective skin depth of SPPs in Au and Ag films with a Ti adhesive layer, we employed the effective medium approximation for thin films and evaluated the effective permittivity as proposed by Aspnes [49]:

$$\varepsilon_{\text{eff}} = f_{\text{Au,Ag}}\varepsilon_{\text{Au,Ag}} + f_{\text{Ti}}\varepsilon_{\text{Ti}}, \quad (9)$$

where f represents the volume fraction (i.e., film thickness ratio) of the corresponding medium. Note that we considered the electron-boundary scattering effects for both Au (or Ag) and Ti layers when estimating their permittivity by using Eq. (5). Since Au and Ag have greater permittivity than Ti, the effective permittivity ε_{eff} decreases proportionally to the film thickness ratio of Au and Ag films. As a consequence, the effective skin depth of Au and Ag films with a Ti adhesive layer is approximately 25% larger (around 15 nm) compared to that of single Au and Ag films (around 12 nm). Furthermore, the effective skin depth exhibits a similar magnitude to the radiation penetration depth at the peak wavelength of the Planck distribution at 300 K ($\approx 10 \mu\text{m}$), which corresponds to about 15 nm.

From our calculations of the plasmon thermal conductivity of Au and Ag films with a Ti adhesive layer, we found that 20 nm is the best thickness for both Au and Ag films. After that, we made the optimized sample by using electron-beam evaporation to deposit Au and Ag films 20 nm thick and a Ti adhesive layer 10 nm thick on a SiO₂ substrate. The deposited films were patterned in circular shapes with various radii ranging from 500 μm to 50 nm, following a similar approach as described in our previous work [34]. We measured the roughness of the Au and Ag film surfaces and found that it was less than 0.5 nm (see Sec. 2 of the Supplemental Material for more information [47]). This showed that the conditions for long-range SPPs could be met. Furthermore, it is known that an Au film with a thickness of 20 nm follows the optical properties predicted by the simple mean free path theory (i.e., Γ_{film} with size effect) [50]. The thicknesses of the Au and Ag films were measured using a stylus profiler (Alpha-Step 500, KLA Tencor Corp.). The measured thicknesses were found to be $22.2 \pm 0.4 \text{ nm}$ for Au films and $20.1 \pm 1.4 \text{ nm}$ for Ag films. To determine the electron thermal conductivity $k_{\parallel,e}$ of the Au and Ag films, we utilized sheet resistances measured via the four-probe method (4200-SCS, Keithley). Both Au and Ag films follow the Wiedemann-Franz law, which states that thermal conductivity and electrical conductivity are proportional, given by the equation

$$\frac{k_{\parallel,e}}{\sigma} = L_m T, \quad (10)$$

where L_m is the Lorentz number for the respective metals. The Lorentz number is known to be $2.51 \times 10^{-8} \text{ W } \Omega \text{ K}^{-2}$ for Au and $2.39 \times 10^{-8} \text{ W } \Omega \text{ K}^{-2}$ for Ag [43]. Here, $\sigma = 1/\rho = 1/(R_s d)$ represents the electrical conductivity, where

TABLE I. Measured values of $k_{\parallel,e}$ from the four-probe method.

Radius (mm)	Au ($d = 22.2 \pm 0.4$ nm)			Ag ($d = 20.1 \pm 1.4$ nm)		
	R_s ($\Omega \text{ sq}^{-1}$)	ρ ($\Omega \text{ m}$)	$k_{\parallel,e}$ ($\text{W m}^{-1} \text{ K}^{-1}$)	R_s ($\Omega \text{ sq}^{-1}$)	ρ ($\Omega \text{ m}$)	$k_{\parallel,e}$ ($\text{W m}^{-1} \text{ K}^{-1}$)
50	3.78	8.41×10^{-8}	81.59	2.94	5.91×10^{-8}	110.42
20	4.27	9.47×10^{-8}	72.38	3.02	6.07×10^{-8}	107.57
10	3.94	8.76×10^{-8}	78.27	2.98	5.99×10^{-8}	108.90
Avg.			77.4 ± 4.7			109.0 ± 1.4

R_s is the sheet resistance and d is the film thickness. Using the measured data of sheet resistance and film thickness, we obtained the electron thermal conductivity of the deposited Au and Ag films as $77.4 \pm 4.7 \text{ W m}^{-1} \text{ K}^{-1}$ and $109.0 \pm 1.4 \text{ W m}^{-1} \text{ K}^{-1}$, respectively. Additionally, since the penetration depth of SPPs into air is greater than $100 \mu\text{m}$, the presence of the native oxide layer on the Au and Ag films does not significantly affect the propagation of long-range SPPs [51].

The plasmon thermal conductivity was measured using the steady-state thermoreflectance method (SSTR) [34,52]. For the measurements, a film with a radius of $500 \mu\text{m}$ served as the calibration sample. By comparing the steady-state temperature rise induced by the pump laser at a heated spot between the measurement sample and the calibration sample, it is possible to extract the change in the in-plane thermal conductivity of the measurement sample caused by the plasmon thermal conductivity. To determine the plasmon thermal conductivity of Au and Ag films, a two-dimensional (2D) heat diffusion model was employed, incorporating the measured data of temperature rise, beam size, film thickness, and bulk thermal conductivity of the films and substrate [34,53]. In the case of Au and Ag films, the phonon thermal conductivity [43] and the measurement sensitivity of the cross-plane thermal conductivity [34] can be considered negligible, thus enabling the utilization of the film thermal conductivity values from Table I within the 2D heat diffusion model. Also, thermal boundary conductance G_b is assumed to be $200 \text{ MW m}^{-2} \text{ K}^{-1}$ [52] due to their low sensitivity in solving the 2D heat diffusion model [34]. The beam sizes of the probe and pump lasers were measured to be 4.8 and $4.7 \mu\text{m}$, respectively, using the knife-edge method [34].

Maintaining consistency in the beam size during the measurement processes is essential, because it determines the heat flux from the heated spot. Hence, we continuously monitored the beam size using a CCD camera during five separate measurements of the largest sample ($L = 50 \text{ mm}$) and the calibration sample ($L = 500 \mu\text{m}$) of Au, as illustrated in Fig. 5(a). By fitting the pixel intensity to a Gaussian distribution, we obtained the relative values of the Gaussian diameter of the lasers in terms of the number of pixels, denoted as n_{1/e^2} . The results indicated that n_{1/e^2} was estimated to be 17.97 ± 0.41 for the largest sample and 18.18 ± 0.75 for the calibration sample. Although the beam sizes of the largest sample were slightly smaller than those of the calibration sample by less than 1%, this difference is expected to have a negligible impact on the temperature rise of the calibration sample within the 2D heat diffusion model. In fact, the measurement data presented in Fig. 5(b) reveal that the temperature rise of the

heated spot in the measurement sample is lower compared to that of the calibration sample. This observation suggests that the change in beam size does not affect the observation of the plasmon thermal conductivity.

Figure 5(b) shows the measured plasmon thermal conductivity ($k_{\parallel,\text{SPP}}$) of two samples: a 20-nm-thick Au film and a 20-nm-thick Ag film, both with a 10-nm-thick Ti adhesive layer on a SiO_2 substrate. Experimental results validate two aspects: (1) the thermal transport via SPPs in thin Au and Ag films and (2) the reduction of the plasmon thermal conductivity due to the size effect of the permittivity of Au and Ag films. Both Au and Ag films exhibit a substantial dependence on the film radius (L). Specifically, the sample

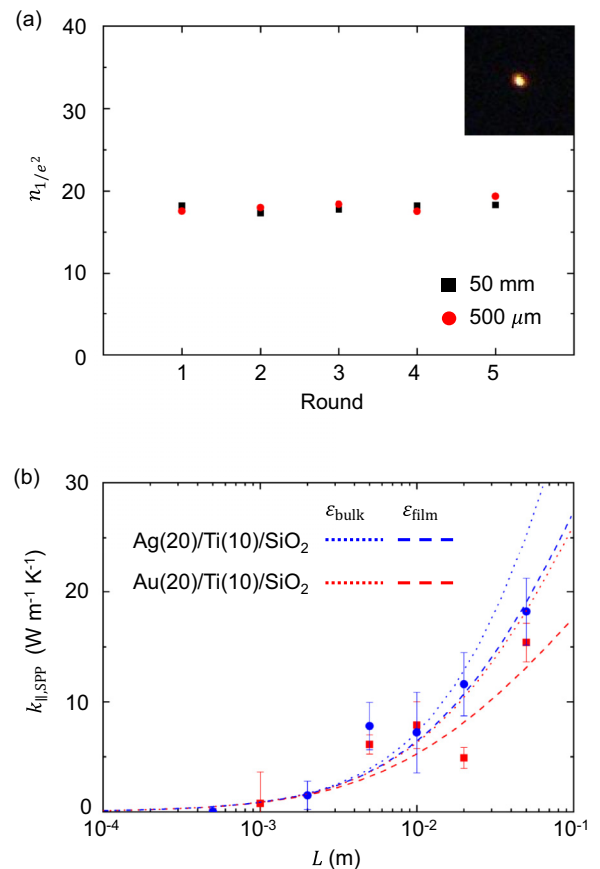


FIG. 5. (a) Number of pixels with intensity over $1/e^2$ (Gaussian diameter) from the beam image of $L = 500 \mu\text{m}$ and $L = 50 \text{ mm}$ samples during five measurements. (b) Measured $k_{\parallel,\text{SPP}}$ with respect to film radius for Au/Ti/SiO₂ and Ag/Ti/SiO₂ samples.

with a 50-mm radius for both Au and Ag films demonstrates a plasmon thermal conductivity of approximately 20% relative to the electron thermal conductivity obtained from Table I. We also conducted measurements for intermediate points where $500 \mu\text{m} < L < 50 \text{ mm}$, which exhibit a discernible trend of increasing values with film width, albeit with some minor scatter. These additional data points serve to bolster the empirical substantiation of the underlying theoretical framework. Moreover, the experimental findings presented in Fig. 5(b) provide compelling evidence that the plasmon thermal conductivity experiences a reduction due to the thickness-dependent characteristics of the permittivity of Au and Ag films. For comparison purposes, theoretical predictions based on the KT, employing ϵ_{bulk} and ϵ_{film} , are also depicted in Fig. 5(b). Notably, the measured data closely align with the theoretical prediction based on the size effect of the metal permittivity. Due to the size effect of the metal permittivity, the theoretical prediction of $k_{\parallel, \text{SPP}}$ at $L = 50 \text{ nm}$ exhibits a decrease of approximately 30% compared to that obtained using ϵ_{bulk} . Furthermore, as illustrated in Fig. 4(a), the calculated plasmon thermal conductivity values for 20-nm-thick Au and Ag films without a Ti adhesive layer amount to almost 30% of their corresponding electron thermal conductivity. The boundary scattering of electrons reduces not only the plasmon thermal conductivity but also the intrinsic thermal conductivity. Thus, the ratio between plasmon and electron thermal conductivities remains relatively constant with respect to the size effect of metallic thin films. Moreover, this corresponding ratio closely resembles that found in the Ti film examined in a previous study by Kim *et al.* [34]. This observation suggests a close relationship between plasmon and electron thermal conductivities in metallic films, possibly

attributed to their mutual dependence on the electron number density, represented as n_e .

IV. CONCLUSION

The SSTR measurements of supported Au and Ag films with a Ti adhesive layer on a SiO_2 substrate provide insights into the thickness and radius dependence of the plasmon thermal conductivity. Through the utilization of the Boltzmann transport equation based on the metal permittivity incorporating the size effect, we determined the optimal thickness of approximately 20 nm for both Au and Ag films to achieve the maximum plasmon thermal conductivity. Importantly, when considering the size effect of the permittivity, the theoretical prediction of the plasmon thermal conductivity experiences a reduction of approximately 30%. For the Au and Ag films with $L = 50 \text{ nm}$, the plasmon thermal conductivity ($k_{\parallel, \text{SPP}}$) exhibits an increase of approximately 20% compared to its electron counterpart. These experimental findings also provide validation for the mean free path theory of the permittivity in the supported structure of Au and Ag thin films. Overall, this paper shows that plasmon thermal conductivity can be used in more real-world situations by using noble metal nanoscale-supported films.

ACKNOWLEDGMENTS

This research is supported by the Basic Science Research Program (Grants No. NRF-2019R1A2C2003605 and No. NRF-2020R1A4A4078930) through the National Research Foundation of Korea funded by Ministry of Science and Information and Communications Technologies ICT.

-
- [1] T. Q. Qiu and C. L. Tien, Heat transfer mechanisms during short-pulse laser heating of metals, *J. Heat Transfer* **115**, 835 (1993).
 - [2] D.-Z. A. Chen, A. Narayanaswamy, and G. Chen, Surface phonon-polariton mediated thermal conductivity enhancement of amorphous thin films, *Phys. Rev. B* **72**, 155435 (2005).
 - [3] C. J. Fu and Z. M. Zhang, Nanoscale radiation heat transfer for silicon at different doping levels, *Int. J. Heat Mass Transf.* **49**, 1703 (2006).
 - [4] J. Ordonez-Miranda, L. Tranchant, T. Tokunaga, B. Kim, B. Palpant, Y. Chalopin, T. Antoni, and S. Volz, Anomalous thermal conductivity by surface phonon-polaritons of polar nano thin films due to their asymmetric surrounding media, *J. Appl. Phys.* **113**, 084311 (2013).
 - [5] J. Ordonez-Miranda, L. Tranchant, Y. Chalopin, T. Antoni, and S. Volz, Thermal conductivity of nano-layered systems due to surface phonon-polaritons, *J. Appl. Phys.* **115**, 054311 (2014).
 - [6] M. Lim, J. Ordonez-Miranda, S. S. Lee, B. J. Lee, and S. Volz, Thermal-conductivity enhancement by surface electromagnetic waves propagating along multilayered structures with asymmetric surrounding media, *Phys. Rev. Appl.* **12**, 034044 (2019).
 - [7] D. Polder and M. Van Hove, Theory of radiative heat transfer between closely spaced bodies, *Phys. Rev. B* **4**, 3303 (1971).
 - [8] J.-J. Greffet, R. Carminati, K. Joulain, J.-P. Mulet, S. Mainguy, and Y. Chen, Coherent emission of light by thermal sources, *Nature (London)* **416**, 61 (2002).
 - [9] E. Rousseau, A. Siria, G. Jourdan, S. Volz, F. Comin, J. Chevrier, and J.-J. Greffet, Radiative heat transfer at the nanoscale, *Nat. Photonics* **3**, 514 (2009).
 - [10] S. Shen, A. Narayanaswamy, and G. Chen, Surface phonon polaritons mediated energy transfer between nanoscale gaps, *Nano Lett.* **9**, 2909 (2009).
 - [11] H. Chalabi, E. Hasman, and M. L. Brongersma, Near-field radiative thermal transfer between a nanostructured periodic material and a planar substrate, *Phys. Rev. B* **91**, 014302 (2015).
 - [12] K. Kim, B. Song, V. Fernández-Hurtado, W. Lee, W. Jeong, L. Cui, D. Thompson, J. Feist, M. T. H. Reid, F. J. García-Vidal, J. C. Cuevas, E. Meyhofer, and P. Reddy, Radiative heat transfer in the extreme near field, *Nature (London)* **528**, 387 (2015).
 - [13] B. Song, D. Thompson, A. Fiorino, Y. Ganjeh, P. Reddy, and E. Meyhofer, Radiative heat conductances between dielectric and metallic parallel plates with nanoscale gaps, *Nat. Nanotechnol.* **11**, 509 (2016).
 - [14] T. Wang, P. Li, D. N. Chigrin, A. J. Giles, F. J. Bezares, O. J. Glembocki, J. D. Caldwell, and T. Taubner, Phonon-polaritonic bowtie nanoantennas: Controlling infrared thermal radiation at the nanoscale, *ACS Photon.* **4**, 1753 (2017).

- [15] A. Fiorino, D. Thompson, L. Zhu, B. Song, P. Reddy, and E. Meyhofer, Giant enhancement in radiative heat transfer in sub-30 nm gaps of plane parallel surfaces, *Nano Lett.* **18**, 3711 (2018).
- [16] W. Li and S. Fan, Nanophotonic control of thermal radiation for energy applications, *Opt. Express* **26**, 15995 (2018).
- [17] M. Lim, J. Song, S. S. Lee, and B. J. Lee, Tailoring near-field thermal radiation between metallo-dielectric multilayers using coupled surface plasmon polaritons, *Nat. Commun.* **9**, 4302 (2018).
- [18] D. G. Baranov, Y. Xiao, I. A. Nechepurenko, A. Krasnok, A. Alù, and M. A. Kats, Nanophotonic engineering of far-field thermal emitters, *Nat. Mater.* **18**, 920 (2019).
- [19] K. Joulain, J.-P. Mulet, F. Marquier, R. Carminati, and J.-J. Greffet, Surface electromagnetic waves thermally excited: Radiative heat transfer, coherence properties and Casimir forces revisited in the near field, *Surf. Sci. Rep.* **57**, 59 (2005).
- [20] A. Giri, S. G. Walton, J. Tomko, N. Bhatt, M. J. Johnson, D. R. Boris, G. Lu, J. D. Caldwell, O. V. Prezhdo, and P. E. Hopkins, Ultrafast and nanoscale energy transduction mechanisms and coupled thermal transport across interfaces, *ACS Nano* **17**, 14253 (2023).
- [21] J. Burke, G. Stegeman, and T. Tamir, Surface-polariton-like waves guided by thin, lossy metal films, *Phys. Rev. B* **33**, 5186 (1986).
- [22] F. Yang, J. Sambles, and G. Bradberry, Long-range surface modes supported by thin films, *Phys. Rev. B* **44**, 5855 (1991).
- [23] L. Tranchant, S. Hamamura, J. Ordonez-Miranda, T. Yabuki, A. Vega-Flick, F. Cervantes-Alvarez, J. J. Alvarado-Gil, S. Volz, and K. Miyazaki, Two-dimensional phonon polariton heat transport, *Nano Lett.* **19**, 6924 (2019).
- [24] Y. Wu, J. Ordonez-Miranda, S. Gluchko, R. Anufriev, D. D. S. Meneses, L. D. Campo, S. Volz, and M. Nomura, Enhanced thermal conduction by surface phonon-polaritons, *Sci. Adv.* **6**, eabb4461 (2020).
- [25] Y. Wu, J. Ordonez-Miranda, L. Jalabert, S. Tachikawa, R. Anufriev, H. Fujita, S. Volz, and M. Nomura, Observation of heat transport mediated by the propagation distance of surface phonon-polaritons over hundreds of micrometers, *Appl. Phys. Lett.* **121**, 112203 (2022).
- [26] S. Tachikawa, J. Ordonez-Miranda, Y. Wu, L. Jalabert, R. Anufriev, S. Volz, and M. Nomura, In-plane surface phonon-polariton thermal conduction in dielectric multilayer systems, *Appl. Phys. Lett.* **121**, 202202 (2022).
- [27] J. Ordonez-Miranda, Y. A. Kosevich, B. J. Lee, M. Nomura, and S. Volz, Plasmon thermal conductance and thermal conductivity of metallic nanofilms, *Phys. Rev. Appl.* **19**, 044046 (2023).
- [28] B. Lamprecht, J. R. Krenn, G. Schider, H. Ditlbacher, M. Salerno, N. Felidj, A. Leitner, F. R. Aussenegg, and J. C. Weeber, Surface plasmon propagation in microscale metal stripes, *Appl. Phys. Lett.* **79**, 51 (2001).
- [29] F. Garcia-Vidal, L. Martin-Moreno, and J. Pendry, Surfaces with holes in them: New plasmonic metamaterials, *J. Opt. A* **7**, S97 (2005).
- [30] A. Hohenau, J. R. Krenn, A. L. Stepanov, A. Drezet, H. Ditlbacher, B. Steinberger, A. Leitner, and F. R. Aussenegg, Dielectric optical elements for surface plasmons, *Opt. Lett.* **30**, 893 (2005).
- [31] A. Krasavin and A. Zayats, Passive photonic elements based on dielectric-loaded surface plasmon polariton waveguides, *Appl. Phys. Lett.* **90**, 211101 (2007).
- [32] G. Baffou, R. Quidant, and F. J. García de Abajo, Nanoscale control of optical heating in complex plasmonic systems, *ACS Nano* **4**, 709 (2010).
- [33] A. Lalis, G. Tessier, J. Plain, and G. Baffou, Plasmonic efficiencies of nanoparticles made of metal nitrides (TiN, ZrN) compared with gold, *Sci. Rep.* **6**, 38647 (2016).
- [34] D.-m. Kim, S. Choi, J. Cho, M. Lim, and B. J. Lee, Boosting thermal conductivity by surface plasmon polaritons propagating along a thin Ti film, *Phys. Rev. Lett.* **130**, 176302 (2023).
- [35] C. Yeh and F. I. Shimabukuro, *The Essence of Dielectric Waveguides* (Springer, New York, 2008).
- [36] M. Galassi, J. Davies, J. Theiler, B. Gough, G. Jungman, P. Alken, M. Booth, F. Rossi, and R. Ulerich, GNU Scientific Library, Vol. 3.
- [37] M. A. Ordal, R. J. Bell, R. W. Alexander, L. L. Long, and M. R. Querry, Optical properties of fourteen metals in the infrared and far infrared: Al, Co, Cu, Au, Fe, Pb, Mo, Ni, Pd, Pt, Ag, Ti, V, and W, *Appl. Opt.* **24**, 4493 (1985).
- [38] M. A. Ordal, R. J. Bell, R. W. Alexander, L. L. Long, and M. R. Querry, Optical properties of Au, Ni, and Pb at submillimeter wavelengths, *Appl. Opt.* **26**, 744 (1987).
- [39] E. D. Palik, *Handbook of Optical Constants of Solids* (Academic, New York, 1998), Vol. 3.
- [40] Y. Guo, S. Tachikawa, S. Volz, M. Nomura, and J. Ordonez-Miranda, Quantum of thermal conductance of nanofilms due to surface-phonon polaritons, *Phys. Rev. B* **104**, L201407 (2021).
- [41] D. Gall, Electron mean free path in elemental metals, *J. Appl. Phys.* **119**, 085101 (2016).
- [42] Z. M. Zhang, *Nano/Microscale Heat Transfer, Mechanical Engineering Series* Vol. 410 (Springer, New York, 2007).
- [43] Z. Tong, S. Li, X. Ruan, and H. Bao, Comprehensive first-principles analysis of phonon thermal conductivity and electron-phonon coupling in different metals, *Phys. Rev. B* **100**, 144306 (2019).
- [44] L. V. Keldysh, Coulomb interaction in thin semiconductor and semimetal films, *JETP Lett.* **29**, 658 (1979).
- [45] I. V. Bondarev and V. M. Shalaev, Universal features of the optical properties of ultrathin plasmonic films, *Opt. Mater. Express* **7**, 3731 (2017).
- [46] D. Shah, M. Yang, Z. Kudyshev, X. Xu, V. M. Shalaev, I. V. Bondarev, and A. Boltasseva, Thickness-dependent Drude plasma frequency in transdimensional plasmonic TiN, *Nano Lett.* **22**, 4622 (2022).
- [47] See Supplemental Material at <http://link.aps.org/supplemental/10.1103/PhysRevB.108.205418> for (1) thickness-dependent plasma frequency of Au and Ag thin films and (2) surface roughness of Au and Ag thin films. It includes Refs. [54–59].
- [48] H. Raether, *Surface Plasmons on Smooth and Rough Surfaces and on Gratings, Springer Tracts in Modern Physics* (Springer, New York, 1988), Vol. 111.
- [49] D. E. Aspnes, Optical properties of thin films, *Thin Solid Films* **89**, 249 (1982).
- [50] O. Stenzel, S. Wilbrandt, S. Stempfhuber, D. Gäbler and S.-J. Wölleb, Spectrophotometric characterization of thin copper and gold films prepared by electron beam evaporation: Thickness

- dependence of the Drude damping parameter, *Coatings* **9**, 181 (2019).
- [51] H. Ditlbacher, J. R. Krenn, G. Schider, A. Leitner, and F. R. Aussenegg, Two-dimensional optics with surface plasmon polaritons, *Appl. Phys. Lett.* **81**, 1762 (2002).
- [52] J. L. Braun, D. H. Olson, J. T. Gaskins, and P. E. Hopkins, A steady-state thermoreflectance method to measure thermal conductivity, *Rev. Sci. Instrum.* **90**, 024905 (2019).
- [53] J. L. Braun and P. E. Hopkins, Upper limit to the thermal penetration depth during modulated heating of multilayer thin films with pulsed and continuous wave lasers: A numerical study, *J. Appl. Phys.* **121**, 175107 (2017).
- [54] A. Catellani and A. Calzolari, Plasmonic properties of refractory titanium nitride, *Phys. Rev. B* **95**, 115145 (2017).
- [55] A. Rodríguez Echarri, J. D. Cox, and F. J. García de Abajo, Quantum effects in the acoustic plasmons of atomically thin heterostructures, *Optica* **6**, 630 (2019).
- [56] A. Manjavacas and F. García de Abajo, Tunable plasmons in atomically thin gold nanodisks, *Nat. Commun.* **5**, 3548 (2014).
- [57] A. Politano, V. Formoso, and G. Chiarello, Dispersion and damping of gold surface plasmon, *Plasmonics* **3**, 165 (2008).
- [58] A. Politano, V. Formoso, and G. Chiarello, Dispersion and damping of surface plasmon in Ag thin films grown on Cu (111) and Ni (111), *Superlattices Microstruct.* **46**, 137 (2009).
- [59] M. Etxebarria, T. Escuin, M. Vinas, and C. Ascaso, Useful surface parameters for biomaterial discrimination, *Scanning* **37**, 429 (2015).